

The chemical signature of the Galactic spiral arms revealed by Gaia DR3

E. Poggio^{1,2}, A. Recio-Blanco¹, P. A. Palicio¹, P. Re Fiorentin², P. de Laverny¹, R. Drimmel², G. Kordopatis¹, M. G. Lattanzi², M. Schultheis¹, A. Spagna², and E. Spitoni¹

¹ Université Côte d'Azur, Observatoire de la Côte d'Azur, CNRS, Laboratoire Lagrange, France
e-mail: poggio.eloisa@gmail.com

² Osservatorio Astrofisico di Torino, Istituto Nazionale di Astrofisica (INAF), I-10025 Pino Torinese, Italy

Received XXXX; accepted YYY

ABSTRACT

Taking advantage of the recent *Gaia* Data Release 3 (DR3), we map chemical inhomogeneities in the Milky Way's disc out to a distance of ~ 4 kpc of the Sun, using different samples of bright giant stars ($\log(g) < 1.5$ dex, $T_{\text{eff}} \sim 3500 - 5500$ K). We detect remarkable inhomogeneities, which appear to be more prominent and structured for the sample containing stars with relatively hotter effective temperatures. For this sample, we identify three (possibly four) metal-rich elongated features in the Galactic plane, which are located in proximity of the spiral arms in the Galactic disc. When projected onto Galactic radius, those features manifest themselves as statistically significant bumps on top of the observed radial gradients, making the assumption of a linear radial decrease not applicable to this sample. In contrast, the sample containing cooler giants exhibits a relatively smooth decrease as a function of Galactic radius. Considering different slices in Galactic azimuth ϕ , the slope of the measured radial metallicity gradient for the cool giants varies gradually from ~ -0.05 dex kpc^{-1} at $\phi \sim -20^\circ$ to ~ -0.03 dex kpc^{-1} at $\phi \sim 20^\circ$. The strong correlation between the spiral structure of the Galaxy and the observed chemical pattern in the sample with relatively hotter effective temperatures indicates that the spiral arms might be at the origin for the detected chemical inhomogeneities. In this scenario, the spiral arms would leave in the hotter stars a strong signature, which progressively disappears when cooler giants stars are considered.

1. Introduction

It has been known for several decades that the disc of the Milky Way contains large-scale non-axisymmetric features, including the spiral arms and a central bar (see e.g. [Georgelin & Georgelin 1976](#); [Okuda et al. 1977](#); [Shen & Zheng 2020](#); [Gaia Collaboration et al. 2022b](#), and references therein), which can play an important role in the disc's evolution, and are expected to leave their signature in the observed properties of the stars.

Several models tried to explain the behaviour of spiral arms in disk galaxies, although their dynamical nature and physical origin still remain unknown. Spiral arms have been proposed to induce large-scale shock waves that trigger the gravitational collapse of gas clouds, enhancing star formation ([Roberts 1969](#)). They can also induce radial migration of stars ([Lynden-Bell & Kalnajs 1972](#); [Sellwood & Binney 2002](#); [Schönrich & Binney 2009a,b](#); [Roškar et al. 2012](#)), and trap or scatter stars close to orbital resonances ([Contopoulos & Grosbøl 1986](#)). As a consequence, they can generate variations in the mean chemical composition of stars in the arm and inter-arm regions ([Minchev et al. 2012](#); [Kordopatis et al. 2015](#); [Grand et al. 2016](#); [Khoperskov et al. 2018](#); [Spitoni et al. 2019](#); [Khoperskov & Gerhard 2021](#)).

Several works have found evidence of azimuthal variations in the mean chemical composition of stars in external galaxies (e.g. [Sánchez-Menguiano et al. 2016](#); [Ho et al. 2017](#); [Vogt et al. 2017](#)). In the Milky Way, chemical inhomogeneities were explored by several studies. [Balsler et al. \(2011\)](#) analyzed the oxygen distribution of HII regions in the Galactic disc, divided their sample into three Galactic azimuth bins, and found that the corresponding radial gradients were significantly different. Chemical inhomogeneities in iron and oxygen were also found in

Cepheids stars ([Pedicelli et al. 2009](#); [Genovali et al. 2014](#); [Kovtyukh et al. 2022](#)). Large metallicity variations were also found in the interstellar medium ([De Cia et al. 2021](#)). By combining data from HII regions, Cepheids, B stars and red supergiants, [Davies et al. \(2009\)](#) presented evidence for large azimuthal variations (~ 0.4 dex) in oxygen, magnesium and silicon on a scale of few kpc in the inner Galactic disk. On the other hand, using APOGEE red-clump stars, [Bovy et al. \(2014\)](#) constrained azimuthal variations in the median metallicity to be ≤ 0.02 dex in the region covered by their sample. Using the large spectroscopic survey RAVE and the Geneva Copenhagen Survey, [Antoja et al. \(2017\)](#) analyzed stars in a cylinder of 0.5 kpc radius centered on the Sun, and found asymmetric metallicity patterns in velocity space.

Recently, *Gaia* Data Release 3 (hereafter DR3, [Gaia Collaboration & Vallenari 2022](#)) published the largest stellar catalog with chemical abundances, atmospheric parameters and radial velocities ever created. Radial Velocity Spectrometer (RVS) data were parameterised by the General Stellar Parameteriser - spectroscopy (*GSP-Spec*) module ([Recio-Blanco et al. 2022](#)), delivering chemo-physical parameters for 5.6 million stars over the entire sky. Thanks to the large number of chemical and astrometric measurements, as well as *Gaia*'s all-sky sampling, it is now possible to map chemical inhomogeneities in the Milky Way's disc as never before, with the goal of detecting the possible signature left by the Galactic spiral arms in the stellar metallicity.

The paper is structured as follows: in Section 2 we describe the datasets; in Section 3 we present our results; in Section 4 we discuss our findings and future perspectives.

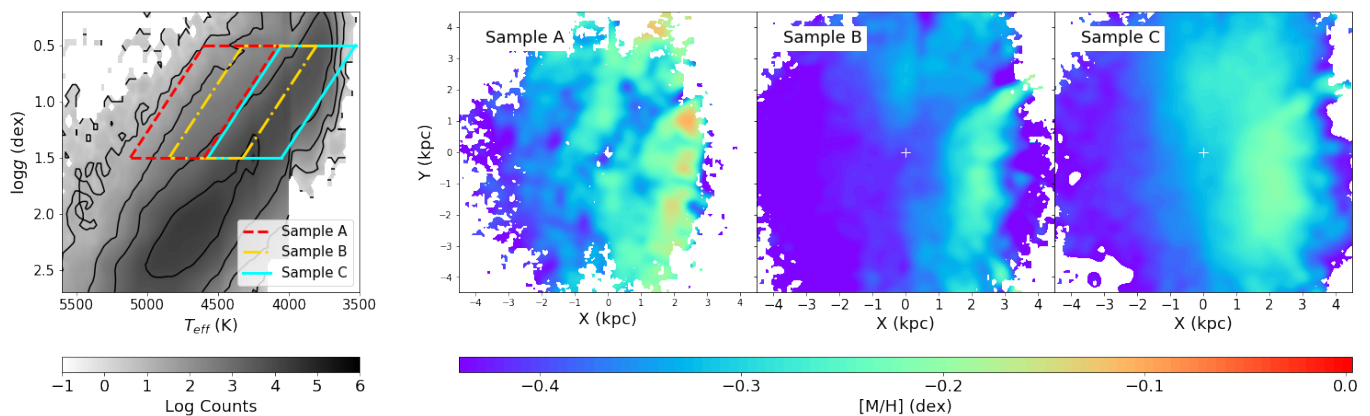


Fig. 1. Chemical inhomogeneities in the Galactic disc for three different samples. Left panel: Selection of Sample A, B and C in the Kiel diagram. Right panels: Mean metallicity in heliocentric coordinates for Sample A, B, and C (from left to right) in the Galactic plane. The position of the Sun is shown by the white cross in $(X, Y) = (0 \text{ kpc}, 0 \text{ kpc})$; the Galactic center is to the right; Galactic rotation is going clockwise.

2. Data selection

In this study, we use the main atmospheric parameters (effective temperature T_{eff} , stellar surface gravity $\log(g)$, global metallicity $[M/H]$) derived from *Gaia* RVS spectra by the *GSP-Spec* module, to select tracers of the disc population and map large-scale chemical inhomogeneities in our Galaxy. The quality constraints on spectroscopic and astrometric measurements (as well as a Toomre kinematical selection) are detailed in Appendix A.

To serve our purpose, we focus on giant stars, as they are intrinsically bright, and therefore allow us to sample a relatively large volume of the Galactic disc. Also, a robust statistical analysis can be performed, taking advantage of the large number of high-quality chemical measurements for these stars¹, thanks to high signal-to-noise spectra.

Figure 1 (left panel) shows the portion of the Kiel diagrams populated by the giant stars in our selected sample. Here we select stars brighter than the red clump (which is located at approximately $\log(g) \approx 2.3$ and $T_{\text{eff}} \approx 4750 \text{ K}$, see Fig. 1), to avoid selection function effects due to the superposition of different stellar populations (see Section 4 of Gaia Collaboration et al. 2022c). Indeed, such effects can cause artifacts when investigating radial gradients, which might be erroneously interpreted as signatures of the spiral arms. Selected areas in Fig. 1 (left panel) define three different subsamples (details in Appendix A), which cover different portions of the red giant branch. Additionally, we apply a vertical cut $|Z| = |d \sin b| < 0.75 \text{ kpc}$, where b is the galactic latitude and d is the heliocentric distance according to the geometric model by Bailer-Jones et al. (2021). The adopted samples are here labelled as A, B, and C, and contain respectively 19 340, 151 139, and 346 570 stars.

The portion of the Kiel diagram covered by our three samples is expected to be populated by stars of different ages. Both theoretical considerations (based on isochrones) and empirical evidence (based on spatial distribution and stellar kinematics) indicate that Sample A is expected to be typically younger than the other two samples (more details in Appendix B). As will be shown in the following, the different content of the three samples will determine remarkable differences in their observed metallicity maps.

¹ As an indication, for stars with $\log(g) < 2.5$ and $6000 < T_{\text{eff}} < 3500 \text{ K}$, the metallicity uncertainty is $< 0.1 \text{ dex}$ for 1.4 million stars, $< 0.05 \text{ dex}$ for $\sim 680\,000$ stars, and $< 0.01 \text{ dex}$ for $\sim 43\,000$ stars.

3. Results

Figure 1 (right panels) shows the maps of the mean metallicity $\langle [M/H] \rangle$ in the Galactic plane for Samples A, B and C, using a smoothing Gaussian kernel with a bandwidth of 175 pc (see Appendix C). We observe that the three maps exhibit both similarities and differences, as discussed in the following. On a large scale, stars are typically more metal rich toward the inner parts of the Galaxy for all three samples. This is in agreement with previous observations of radial metallicity gradients in the Galactic disc (e.g. Genovali et al. 2014; Gaia Collaboration et al. 2022c), and also expected from the inside-out formation scenario (Bird et al. 2013; Matteucci 2021). However, the samples also present smaller-scale metallicity inhomogeneities. The relative importance, extent, and shape of the observed inhomogeneities vary for the three different samples. Sample A exhibits three, possibly four, metal-rich elongated features, that diagonally cross the Galactic plane, approximately from the upper right to the lower left corner of the figure. This pattern becomes progressively less evident as we move from Sample A to Sample B and C. In Sample C, the elongated features disappear almost completely, and simply result in an observed asymmetry about the Sun of stars at $X \approx 0 \text{ kpc}$, typically more metal rich at $Y > 0 \text{ kpc}$ than at $Y < 0 \text{ kpc}$. While such asymmetry was already noted by Gaia Collaboration et al. (2022c) in their RGB sample, the scenario presented in this contribution indicates that it might represent a remnant of the spiral arms chemical signature.

Figure 2 (upper left panel) shows again the mean metallicity for Sample A, but now compared to the position of the spiral arms in the Galaxy as mapped by Upper Main Sequence stars in Poggio et al. (2021) (hereafter P21), shown as grey shaded areas and black contours, indicating from left to right segments of: the Perseus arm, the Local (Orion) arm, and the Sagittarius-Carina (Sag-Car) arm (the latter contour being possibly containing the Scutum arm).

In the right panel of Figure 2, we can see the spatial distribution of sources in Sample A, obtained with an Epanechnikov kernel density estimator with a bandwidth of 250 pc. White contours show again the position of the nearest spiral arms from Upper Main Sequence stars. As we can see, Sample A traces well the position of the spiral arms, confirming that it contains typically young stars.

To better analyse and map chemical inhomogeneities in the Galactic disc, we define a new variable, called Metallicity Excess = $\langle [M/H] \rangle_{\text{loc}} - \langle [M/H] \rangle_{\text{large}}$, where $\langle [M/H] \rangle_{\text{loc}}$ and

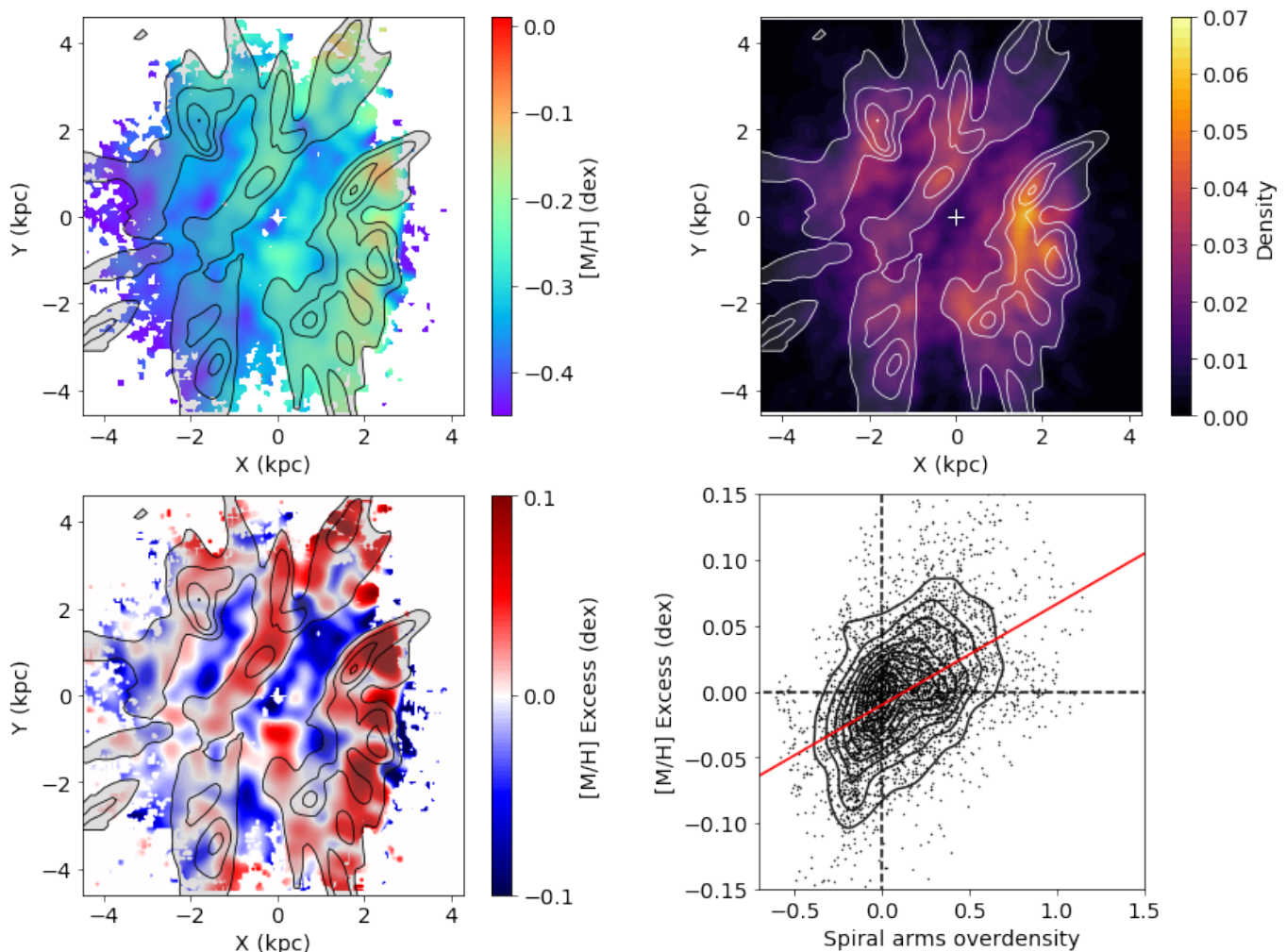


Fig. 2. Correlation between the observed metal-rich features in Sample A and the segments of the nearest spiral arms in the Galaxy. *Left panel:* Map of the mean metallicity in the Galactic plane for Sample A shown in Fig. 1, but now compared to the position of the spiral arms from Upper Main Sequence stars (P21), shown as grey shaded areas. *Middle panel:* Same as left panel, but showing the metallicity excess. Regions with positive (negative) metallicity excess are more metal rich (poor) than the average. (See text for a detailed explanation). *Right panel:* Using the map shown in the middle panel, the overdensity of the spiral arms vs. the metallicity excess is shown for each pixel (shown as black dots). When the spiral arm overdensity is > 0 , the region can be considered belonging to a spiral arm, whereas regions with < 0 can be considered interarm regions. Black contours show the distribution of the pixels in the spiral arms overdensity vs. metallicity excess space. The red line shows a linear fit to the black points.

$\langle [M/H] \rangle_{\text{large}}$ represent the mean metallicity smoothed on a local or large scale, respectively. The smoothing is performed as described in Appendix C. The lower left panel of Figure 2 shows the obtained Metallicity Excess for Sample A if we adopt for the local smoothing the same value chosen for the mean metallicity in the upper left panel of Figure 2 (i.e. $\langle [M/H] \rangle_{\text{loc}} = \langle [M/H] \rangle$), and for the large-scale metallicity a scale-length of 5 times the value adopted for the local smoothing. The red (blue) regions in the Metallicity Excess map should be interpreted as places where the stars are more metal-rich (-poor) than the average. We therefore study the correlation between the observed metal-rich regions and the geometry of the spiral arms by dissecting the middle panel in pixels of 0.3 kpc width. For each pixel, we consider the spiral arms overdensity (calculated as described in P21) and the Metallicity Excess. The correlation between these two quantities is shown in Figure 2 (bottom right panel), with every black dot corresponding to a pixel. The red line shows a linear fit to the black dots. As we can see, regions located in correspondence of the spiral arms (i.e. with overdensity larger

than 0) tend to be more metal rich than the average (i.e. with a Metallicity excess larger than 0). To quantify the correlation between these two variables, we calculate Kendall's correlation coefficient $\tau_B = 0.38$, which can be considered as an indication of strong positive correlation². Therefore, the elongated metal-rich features observed in Sample A appear to be statistically correlated with the position of the spiral arms in the Galaxy.

It should be noted, however, that there are some exceptions. For instance, some regions of the Galactic plane are more metal rich than the average, but they do not coincide with the spiral arms contours (e.g. $(X, Y) = (0 \text{ kpc}, -1 \text{ kpc})$ in Fig. 2, upper and bottom left panel). On the other hand, not all the regions in the spiral arms exhibit the same chemical behaviour: the metallicity excess seems to be typically high in the Sag-Car arm, and in the upper part ($Y > 0$) of the Local arm, but seems to be milder in the

² A correlation is usually considered very weak for values less than 0.10, weak between 0.10 and 0.19, moderate between 0.20 and 0.29, strong for 0.30 or above (Botsch 2011).

Table 1. Radial gradient for Sample C in different azimuthal bins, as shown in Figure 3, assuming a linear model. Only stars with $R > 6.5$ kpc are here considered, to avoid selection effects in the inner regions due to extinction, as well as $R < 11.5$ kpc, to avoid low statistics regions. The corresponding table for Sample A and B is not presented here due to the spiral arms-related metallicity variations, which are invalidating the assumption of a linear model.

ϕ (deg)	Slope (dex kpc^{-1})	Intercept (dex)
-20 ± 5	-0.054 ± 0.001	0.15 ± 0.01
-15 ± 5	-0.052 ± 0.002	0.14 ± 0.01
-10 ± 5	-0.047 ± 0.002	0.09 ± 0.02
-5 ± 5	-0.046 ± 0.002	0.09 ± 0.01
0 ± 5	-0.047 ± 0.001	0.09 ± 0.01
5 ± 5	-0.046 ± 0.001	0.09 ± 0.01
10 ± 5	-0.043 ± 0.001	0.06 ± 0.01
15 ± 5	-0.039 ± 0.001	0.04 ± 0.01
20 ± 5	-0.035 ± 0.002	0.01 ± 0.01

lower part of the Local arm ($Y < 0$) and the Perseus arm ($Y < \simeq 1$ kpc).

Figure 3 shows the impact of the above-described metal-rich features on the observed metallicity gradient in the Galactic disc. To explore the metallicity variations in the disc, we dissect the Galactic plane into slices of 10° width in Galactic azimuth ϕ . For each slice, we then show the median metallicity for Sample A and Sample C. Sample B presents an intermediate behaviour between Sample A and C (here not shown to preserve the clarity of the Figure). As we can see, Sample A presents some peaks of higher metallicity, superimposed on a global decrease as a function of R , here calculated assuming a distance to the Galactic center $R_\odot = 8.249$ (Gravity Collaboration et al. 2021). Using bootstrap uncertainties, the peaks deviate more than 3-sigma from a linear decrease as a function of Galactic radius, indicating that chemical undulations are dominating the radial metallicity gradient. In this context, the observed peaks can be interpreted as the projection on the radial direction of the metal-rich features observed in the XY maps. For Sample C, on the other hand, a relatively smooth decrease of the median metallicity as a function of R is apparent. The slopes of the radial metallicity gradients for different azimuthal bins can be found in Table 1. As we can see, the radial metallicity gradient gradually varies depending on azimuth, and becomes gradually steeper for $\phi < 0^\circ$.

Additional tests to verify the robustness of our results can be found in Appendix E.

4. Discussion and Conclusion

Taking advantage of the new *Gaia* DR3 data, we have mapped the mean metallicity in the Galactic disc out to 3-4 kpc of the Sun for three different samples of bright giant stars. We found evidence of chemical inhomogeneities, which manifest themselves as statistically significant undulations on top of the expected radial metallicity gradients. The appearance and magnitude of the detected inhomogeneities are different for the three considered samples, being more structured and pronounced for the sample containing hotter (and a larger relative fraction of young massive) stars. In this sample, three (possibly four) extended metal rich features are detected, which appear to be statistically correlated with the position of the spiral arms (independently derived from previous works). Such connection points to the spiral arms as a plausible origin for the observed metal-rich features.

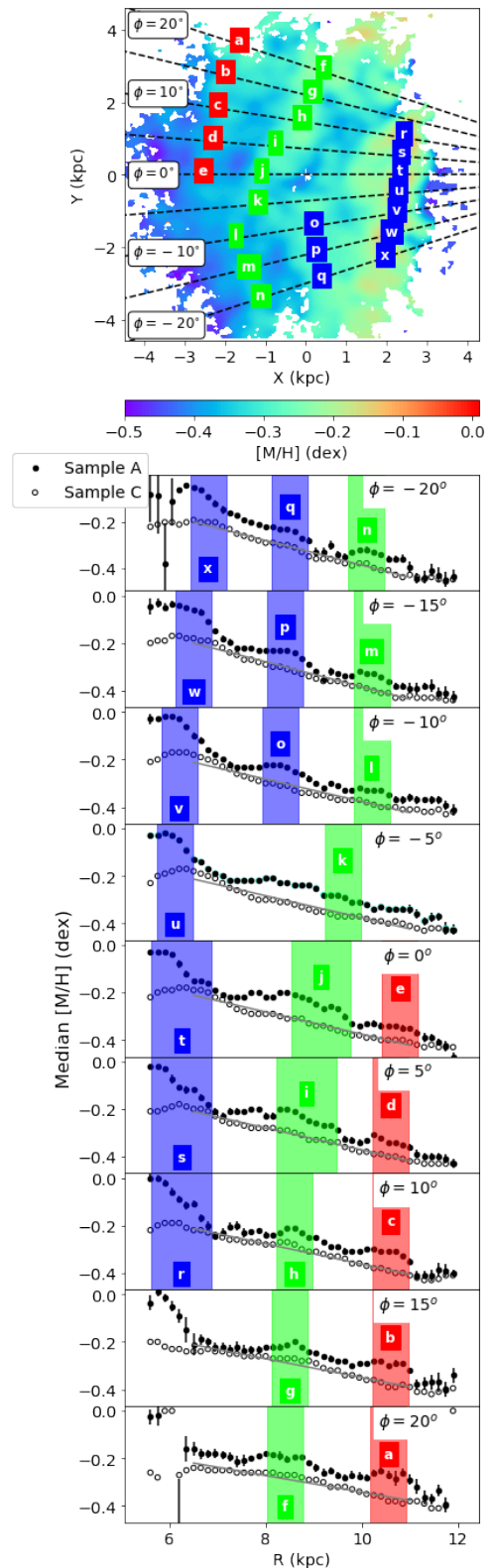


Fig. 3. Impact of the observed chemical inhomogeneities on the Galactic gradients. Upper panel: Map of the mean metallicity in the Galactic plane for Sample A, with overlaid azimuthal slices of 5° , from $\phi = -20^\circ$ to from $\phi = 20^\circ$. Lower panels: median metallicity as a function of Galactocentric radius R for different slices in Galactic azimuth ϕ for Sample A (black dots) and Sample C (open circles). Regions that might be associated with the Perseus (red, letters ‘a’-‘e’), Local (green, ‘f’-‘n’), and Sagittarius/Scutum (blue, ‘o’-‘x’) arms are shown as colored regions both in the upper and lower panels.

Our maps of the mean metallicity in the Milky Way's disc are in good agreement with previous results obtained for external spiral galaxies. For instance, the chemical enrichment of the interstellar medium was found to proceed preferentially along spiral structures, and less efficiently across them in the galaxy HCG91c (Vogt et al. 2017).

Several works available in literature can offer a theoretical framework for the observational results obtained in this work. Using high-resolution N-body simulations, Khoperskov et al. (2018) showed that kinematically hot and cold stellar populations in the Galactic disc react in a different way to a spiral arm perturbation, naturally leading to azimuthal variations in the mean metallicity of stars in the simulated disk (based on the assumption that younger stars typically tend to have higher metallicity and smaller random motions than the older stellar components, see for example Holmberg et al. 2007). Fig. 4 in Khoperskov et al. (2018) shows the observed metallicity variations at different times of the simulation for three different initial metallicity profiles. They found that the spiral arm locii typically tend to be more metal-rich than the interarm-regions. Their predictions are in good agreement with the observations presented in this work.

A detailed modelling of the processes at work in the Galactic disk is therefore crucial to fully explain the observational results presented in this work. Chemo-dynamical evolution models should be adopted to interpret the impact of the spiral arms on disk chemical variations in the Galactic disk, and how different mechanisms can influence the observed present-day chemical abundance patterns (e.g. Roškar et al. 2012; Grand et al. 2016; Minchev et al. 2018; Spitoni et al. 2019; Carr et al. 2022). Future works comparing observations from Gaia DR3 and ground-based surveys to sophisticated theoretical models will be able to show further insights on the evolutionary processes that shaped the present-day appearance of the Milky Way's disk.

Acknowledgements. This work has made use of data from the European Space Agency (ESA) mission Gaia (<https://www.cosmos.esa.int/gaia>), processed by the Gaia Data Processing and Analysis Consortium (DPAC, <https://www.cosmos.esa.int/web/gaia/dpac/consortium>). Funding for the DPAC has been provided by national institutions, in particular the institutions participating in the Gaia Multilateral Agreement. EP acknowledges support by the Centre National d'études Spatiales (CNES). ARB and ES received funding from the European Union's Horizon 2020 research and innovation program under SPACE-H2020 grant agreement number 101004214 (EXPLORE project).

References

Antoja, T., Kordopatis, G., Helmi, A., et al. 2017, *A&A*, 601, A59
 Bailer-Jones, C. A. L., Rybizki, J., Fouvras, M., Demleitner, M., & Andrae, R. 2021, *AJ*, 161, 147
 Balsler, D. S., Rood, R. T., Bania, T. M., & Anderson, L. D. 2011, *ApJ*, 738, 27
 Bensby, T., Feltzing, S., & Lundström, I. 2003, *A&A*, 410, 527
 Bensby, T., Feltzing, S., & Oey, M. S. 2014, *A&A*, 562, A71
 Bird, J. C., Kazantzidis, S., Weinberg, D. H., et al. 2013, *ApJ*, 773, 43
 Botsch, R. 2011, *Scopes and Methods of Political Science*
 Bovy, J., Nidever, D. L., Rix, H.-W., et al. 2014, *ApJ*, 790, 127
 Bressan, A., Marigo, P., Girardi, L., et al. 2012, *MNRAS*, 427, 127
 Carr, C., Johnston, K. V., Laporte, C. F. P., & Ness, M. K. 2022, arXiv e-prints, arXiv:2201.04133
 Chen, Y., Bressan, A., Girardi, L., et al. 2015, *MNRAS*, 452, 1068
 Chen, Y., Girardi, L., Bressan, A., et al. 2014, *MNRAS*, 444, 2525
 Contopoulos, G. & Grosbøl, P. 1986, *A&A*, 155, 11
 Davies, B., Origlia, L., Kudritzki, R.-P., et al. 2009, *ApJ*, 696, 2014
 De Cia, A., Jenkins, E. B., Fox, A. J., et al. 2021, *Nature*, 597, 206
 Gaia Collaboration, Creevey, O. L., Sarro, L. M., et al. 2022a, arXiv e-prints, arXiv:2206.05870
 Gaia Collaboration, Drimmel, R., Romero-Gomez, M., et al. 2022b, arXiv e-prints, arXiv:2206.06207
 Gaia Collaboration, Recio-Blanco, A., Kordopatis, G., et al. 2022c, arXiv e-prints, arXiv:2206.05534

Gaia Collaboration & Vallenari, A. 2022, *A&A* in prep.
 Genovali, K., Lemasle, B., Bono, G., et al. 2014, *A&A*, 566, A37
 Georgelin, Y. M. & Georgelin, Y. P. 1976, *A&A*, 49, 57
 Grand, R. J. J., Springel, V., Kawata, D., et al. 2016, *MNRAS*, 460, L94
 Gravity Collaboration, Abuter, R., Amorim, A., et al. 2021, *A&A*, 654, A22
 Ho, I. T., Seibert, M., Meidt, S. E., et al. 2017, *ApJ*, 846, 39
 Holmberg, J., Nordström, B., & Andersen, J. 2007, *A&A*, 475, 519
 Khoperskov, S., Di Matteo, P., Haywood, M., & Combes, F. 2018, *A&A*, 611, L2
 Khoperskov, S. & Gerhard, O. 2021, arXiv e-prints, arXiv:2111.15211
 Kordopatis, G., Binney, J., Gilmore, G., et al. 2015, *MNRAS*, 447, 3526
 Kordopatis, G., Schultheis, M., McMillan, P. J., et al. 2022, arXiv e-prints, arXiv:2206.07937
 Kovtyukh, V., Lemasle, B., Bono, G., et al. 2022, *MNRAS*, 510, 1894
 Lynden-Bell, D. & Kalnajs, A. J. 1972, *MNRAS*, 157, 1
 Matteucci, F. 2021, *A&A Rev.*, 29, 5
 Minchev, I., Anders, F., Recio-Blanco, A., et al. 2018, *MNRAS*, 481, 1645
 Minchev, I., Famaey, B., Quillen, A. C., et al. 2012, *A&A*, 548, A126
 Okuda, H., Maihara, T., Oda, N., & Sugiyama, T. 1977, *Nature*, 265, 515
 Pastorelli, G., Marigo, P., Girardi, L., et al. 2019, *MNRAS*, 485, 5666
 Pedicelli, S., Bono, G., Lemasle, B., et al. 2009, *A&A*, 504, 81
 Poggio, E., Drimmel, R., Cantat-Gaudin, T., et al. 2021, *A&A*, 651, A104
 Poggio, E., Drimmel, R., Lattanzi, M. G., et al. 2018, *MNRAS*, 481, L21
 Re Fiorentin, P., Lattanzi, M. G., & Spagna, A. 2019, *MNRAS*, 484, L69
 Re Fiorentin, P., Spagna, A., Lattanzi, M. G., & Cignoni, M. 2021, *ApJ*, 907, L16
 Recio-Blanco, A., de Laverny, P., Palicio, P. A., et al. 2022
 Roberts, W. W. 1969, *ApJ*, 158, 123
 Roškar, R., Debattista, V. P., Quinn, T. R., & Wadsley, J. 2012, *MNRAS*, 426, 2089
 Sánchez-Menguiano, L., Sánchez, S. F., Kawata, D., et al. 2016, *ApJ*, 830, L40
 Schönrich, R. & Binney, J. 2009a, *MNRAS*, 396, 203
 Schönrich, R. & Binney, J. 2009b, *MNRAS*, 399, 1145
 Schönrich, R., Binney, J., & Dehnen, W. 2010, *MNRAS*, 403, 1829
 Sellwood, J. A. & Binney, J. J. 2002, *MNRAS*, 336, 785
 Shen, J. & Zheng, X.-W. 2020, *Research in Astronomy and Astrophysics*, 20, 159
 Spitoni, E., Cescutti, G., Minchev, I., et al. 2019, *A&A*, 628, A38
 Tang, J., Bressan, A., Rosenfield, P., et al. 2014, *MNRAS*, 445, 4287
 Vogt, F. P. A., Pérez, E., Dopita, M. A., Verdes-Montenegro, L., & Borthakur, S. 2017, *A&A*, 601, A61
 Zari, E., Rix, H. W., Frankel, N., et al. 2021, *A&A*, 650, A112

Appendix A: Data quality cuts and selection

We select Gaia DR3 sources with atmospheric parameters (available through the *astrophysical_parameters* table), radial velocities, and 5-parameters astrometric solution having quality index $ruwe < 1.4$ (Lindegren 2018). In addition, *Gaia* duplicated sources are excluded from the sample. As for the *GSP-Spec* parameters, we reject objects based on their metallicity uncertainty and *GSP-Spec* quality flags (Recio-Blanco et al. 2022) reporting on the degree of biases from line broadening and radial velocity errors affecting $[M/H]$, flux noise, extrapolation on stellar atmospheric parameters, as well as KM-type stars.

The definition of the working sample is as follows:

```
[M/H]_unc<0.5 & vbroadM<2 & vradM<2 &
fluxNoise<4 & extrapol<3 & KMtypestars<2
astrometric_params_solved = 31 & ruwe < 1.4
& duplicated_source == false
```

From the Gaia archive the following query provides the data set employed:

```
SELECT g*., ap.teff_gspspec,
ap.logg_gspspec, ap.mh_gspspec
FROM gaiadr3.gaia_source AS g
INNER JOIN gaiadr3.astrophysical_parameters AS ap
ON g.source_id = ap.source_id
WHERE (
((mh_gspspec_upper-mh_gspspec_lower)<0.25)
AND ((flags_gspspec LIKE "__0%")
OR (flags_gspspec LIKE "__1%"))
AND ((flags_gspspec LIKE "____0%")
OR (flags_gspspec LIKE "____1%"))
AND ((flags_gspspec LIKE "_____0%")
OR (flags_gspspec LIKE "_____1%")
OR (flags_gspspec LIKE "_____2%")
OR (flags_gspspec LIKE "_____3%"))
AND ((flags_gspspec LIKE "_______0%")
OR (flags_gspspec LIKE "_______1%")
OR (flags_gspspec LIKE "_______2%"))
AND ((flags_gspspec LIKE "_______0%")
OR (flags_gspspec LIKE "_______1%"))
) AND g.astrometric_params_solved== 31
AND g.ruwe < 1.4
```

Additionally, objects without r_{Geo} distances were discarded.

For the obtained sample, we calculate the Galactocentric coordinates R , ϕ , Z and the corresponding velocities V_R , V_ϕ , V_Z following the same conventions and parameters adopted in [Gaia Collaboration et al. \(2022c\)](#). We apply a cut $|Z| < 0.75$ kpc, as we are mainly interested in selecting disc stars. To this end, we also apply a kinematic cut based on the Toomre diagram (see for example [Bensby et al. 2003, 2014](#); [Re Fiorentin et al. 2019, 2021](#); [Gaia Collaboration et al. 2022c,a](#)) in order to remove possible halo contaminants:

$$\sqrt{V_R^2 + V_Z^2 + (V_\phi - V_0)^2} < 210 \text{ km s}^{-1}, \quad (\text{A.1})$$

where $V_0 = 238.5 \text{ km s}^{-1}$ is the velocity of the local standard of rest at the Sun's position, based on [Gravity Collaboration et al. \(2021\)](#); [Schönrich et al. \(2010\)](#).

Finally, we select different populations of RGB stars in the $\log(g)$ - T_{eff} plane of the Kiel diagram. This is accomplished by

selecting stars in the three boxes shown in the left panel of Fig. 1, that is:

$$\begin{aligned} &\log g < 1.5 \ \& \ \log g > 0.5 \ \& \\ &(\log g > (\text{coeff} \cdot \text{teff} + \text{interc_left})) \ \& \\ &(\log g < (\text{coeff} \cdot \text{teff} + \text{interc_right})) \end{aligned}$$

where $\text{coeff} = 0.00192 \text{ K}^{-1}$ is the adopted slope, chosen to follow the natural inclination of the RGB branch (as done also for the selection of the massive sample in [Gaia Collaboration et al. 2022c](#)), whereas the intercept of the two inclined lines, delimiting the selected regions on the left and right side, are: $\text{interc_left} = -8.3 + \Delta$ and $\text{interc_right} = -7.3 + \Delta$, where $\Delta = 0, 0.5$ and 1 for Sample A, B and C, respectively.

Appendix B: Sample characterization

In this section, we perform some tests to further explore the content of Sample A, B and C. First of all, we compare our selected areas of the Kiel diagram with the prediction from the PARSEC isochrones for different metallicities ([Bressan et al. 2012](#); [Chen et al. 2014, 2015](#); [Tang et al. 2014](#); [Pastorelli et al. 2019](#)). Figure B.1 shows the isochrones for 10 Gyr, 1 Gyr, 500 Myr, 100 Myr, 30 and 20 Myr, for both solar metallicity $[M/H]=0$ dex and $[M/H]=-0.5$ dex. It should be noted that effective temperatures from *GSP-Spec* have been found to be in agreement with those from the isochrones (see Sec. 10.2 of [Recio-Blanco et al. 2022](#)), and no important bias has been found with the literature. As we can see in Figure B.1, in the region covered by Sample A, only isochrones for 100 Myr or younger are present. Of course, in real data, we do expect some contamination from older stars, given that uncertainties will tend to blur the distribution. Nevertheless, the fact that Sample B and C contain stars typically older than those in Sample A is supported by the location of the isochrones in the Kiel diagram.

Further indications can be also found empirically. Although ages can be also inferred for stars (e.g. [Kordopatis et al. 2022](#)), here we simply use stellar kinematics as a proxy for the typical age of the sample. For Sample A, B and C, respectively, the velocity dispersions are: $\sigma_{V_Z} = (19.5, 21.8, 23.6) \text{ km/s}$, $\sigma_{V_R} = (28.6, 35.1, 38.9) \text{ km/s}$, $\sigma_{V_{\phi i}} = (26.6, 26.9, 29.0) \text{ km/s}$. Figure B.2 shows the distribution of the azimuthal velocities V_ϕ . As we can see, the distribution of stars in Sample A presents a prominent peak at high azimuthal velocity (~ 230 - 240 km/s). On the contrary, Sample B and Sample C present a broader distribution, with a large fraction of stars at low V_ϕ , as would be expected as a consequence of the asymmetric drift for a kinematically hot stellar population.

Appendix C: Bivariate smoothing

For a given position (X, Y) in the Galactic plane, we calculate the local smoothed metallicity:

$$\langle [M/H] \rangle_{loc}(X, Y) = \frac{\sum_i^N [M/H]_i K\left(\frac{X-X_i}{h_x}\right) K\left(\frac{Y-Y_i}{h_y}\right)}{\sum_i^N K\left(\frac{X-X_i}{h_x}\right) K\left(\frac{Y-Y_i}{h_y}\right)}, \quad (\text{C.1})$$

where N is the total number of stars in the sample, X_i and Y_i are the X- and Y-coordinates of the i -th star of the sample, K is a Gaussian kernel

$$K\left(\frac{X-X_i}{h_x}\right) = \frac{1}{\sqrt{2\pi} h_x} \exp\left(-\frac{1}{2} \left(\frac{X-X_i}{h_x}\right)^2\right) \quad (\text{C.2})$$

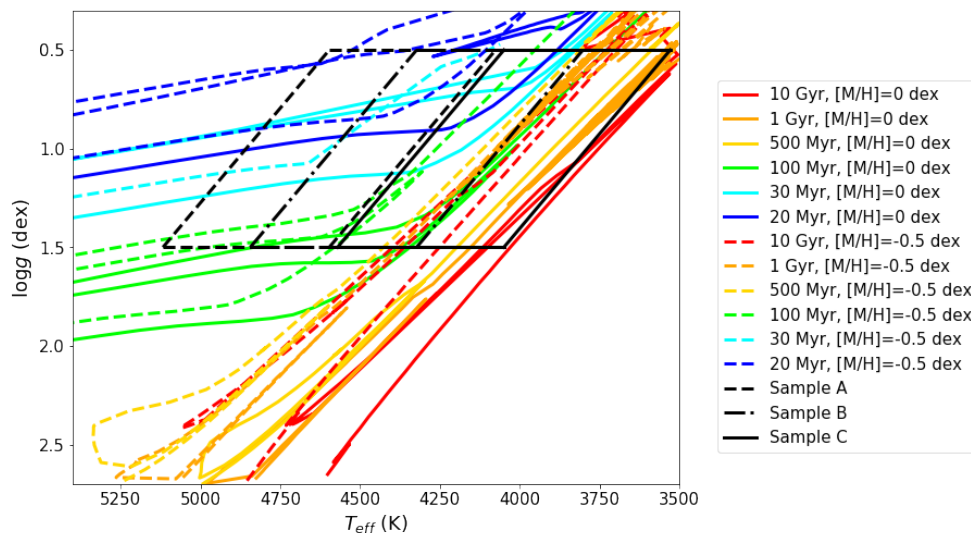


Fig. B.1. PARSEC isochrones for different metallicities, compared to the regions of the Kiel diagram selected here for Sample A, B and C.

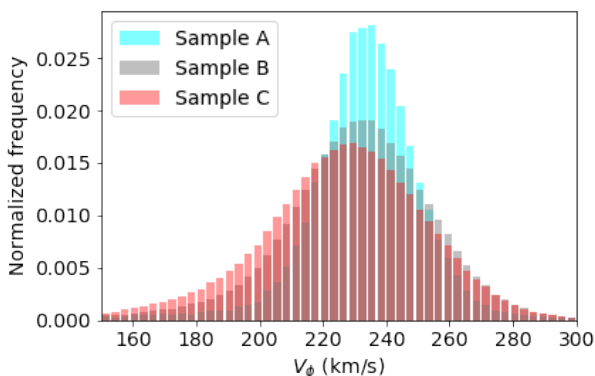


Fig. B.2. Distribution of azimuthal velocities V_ϕ for Samples A, B, and C. The histogram is normalized so that the area under the histogram integrates to 1 for all three samples.

with a scale-length h_X (and similarly for the Y-coordinate). In this work, local smoothed metallicity (see Fig. 1, right panels) is shown using a scale-length of 0.175 kpc. As discussed in the main text, the metallicity excess is calculated by taking the difference of the local metallicity (i.e. Equation C.1, assuming a scale-length of 0.175 kpc) and the metallicity on a large scale (i.e. again using Equation C.1, but now adopting a scale-length 5 times larger than the one used for the local metallicity).

Appendix D: Azimuthal variations

Figure D.1 shows a projection of the observed metal-rich spiral features when the Galactic plane is cut into Galactocentric rings. For each ring, we show the azimuthal variations for both Sample A and Sample C, calculated as the median metallicity as a function of azimuth, after subtracting the median metallicity of the sample in each ring. We note that the azimuthal variations depend on the adopted sample, being more prominent for Sample A; typically, they do not exceed 0.08 dex. The amplitude and location of the observed peaks depend on how the rings are selected with respect to the spiral arms' geometry.

Appendix E: Additional tests

In this Section, we present some additional tests that we perform to verify the robustness of our results.

First, we checked the quality of the astrometric measurements in our selected stars. For Sample A, 99.7 % of the stars have a parallax signal-to-noise greater than 5. For those stars, as a further check, we constructed a map using distances inferred by the inverse of the parallax, obtaining consistent results.

As an additional test, we selected only the stars satisfying the criteria on *Gaia* DR3 astrophysical parameters listed for the high-quality sample in [Gaia Collaboration et al. \(2022c\)](#). In this case, the chemical signature of the spiral arms is still present, but the entire map is shifted toward more metal-rich values, as expected (given that more metal-rich stars are more likely to be included in the high-quality sample).

To test the possible contribution from Asymptotic Giant Branch (AGB) stars, we cross-matched our three samples with the long-period variables catalog available in *Gaia* DR3 `gaiadr3.vari_long_period_variable`. We found that, for all three samples, the percentage of AGB stars from that catalog is less than 0.2 %.

Our maps are also quite robust against the selection of the regions in the Kiel diagram. Indeed, a change in the shape of the selection leave the maps almost unchanged - although, of course, a significant shift in T_{eff} (or $\log(g)$) can make an impact, as discussed in the main text.

Finally, we test other spiral arms maps. The spiral arms contours used in the main text are from the paper P21, which relies on distances calculated as described in [Poggio et al. \(2018\)](#). As a test, we also used the spiral arms overdensity map from [Gaia Collaboration et al. \(2022b\)](#), where the r_{Geo} distances are adopted from [Bailer-Jones et al. \(2021\)](#), as well as the one based the sample from [Zari et al. \(2021\)](#) (which used astro-kinematic distances), always obtaining consistent results.

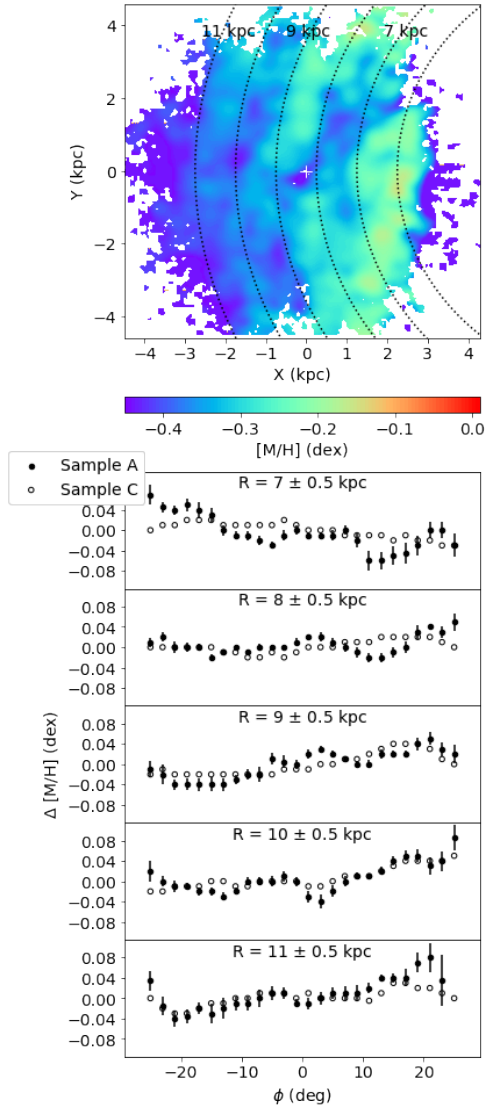


Fig. D.1. *Impact of the observed chemical inhomogeneities on azimuthal variations.* Upper panel: Map of the mean metallicity in the Galactic plane for Sample A, with overlaid rings of constant Galactocentric radius at $R = 6, 7, 8, 9, 10$ and 11 kpc. Lower panels: median metallicity as a function of Galactic azimuth ϕ for different rings in R (as specified in the title of each panel), after the median metallicity of the stars for each ring is subtracted.